Response of Global Tropical Cyclone Activity to Increasing CO_2: Results from Downscaling CMIP6 Models

Kerry Emanuel[1]

Lorenz Center

Massachusetts Institute of Technology

Revised July, 2020

[1] *Corresponding author address and email*: Rm 54-1814, MIT; 77 Massachusetts Avenue, Cambridge, MA 02139. Phone: 617-253-2462. Email: emanuel@mit.edu

Abstract

Global models comprising the sixth generation Coupled Climate Model Intercomparison Project (CMIP6) are downscaled using a very high resolution but simplified coupled atmosphere-ocean tropical cyclone model, as a means of estimating the response of global tropical cyclone activity to increasing greenhouse gases. As with a previous downscaling of CMIP5 models, the results show an increase in both the frequency and severity of tropical cyclones, robust across the models downscaled, in response to increasing greenhouse gases. The increase is strongly weighted to the northern hemisphere, and especially noteworthy is a large increase in the higher latitudes of the North Atlantic. Changes are insignificant in the South Pacific across metrics. Although the largest increases in track density are far from land, substantial increases in global landfalling power dissipation are indicated. The incidence of rapid intensification increases rapidly with warming, as predicted by existing theory. Measures of robustness across downscaled climate models are presented, and comparisons to tropical cyclones explicitly simulated in climate models are discussed.

1. Introduction

The cost to society of climate change is driven largely by the costs associated with extreme climate events such as droughts, floods, wildfires, and storms. Slow changes in long-term average conditions, such as annual mean temperature and sea level, can often be accommodated through an equivalently slow adaptation, but adaptation to changes in infrequent events is notoriously flawed and often unduly influenced by politics and special interests (Gaul, 2019), making each event disproportionately expensive.

The long-term average annual cost, C, of discrete climate events can be defined as the integral of the cost of each event multiplied by the annual probability density of that event, over the whole range of possible costs:

$$C = \int_0^\infty c(i)\,p(i)di, \tag{1}$$

where c is the cost of an event of intensity i, and $p(i)$ is the probability density (probability per unit intensity) associated with that cost.

For extreme events such as tropical cyclones, the cost typically rises steeply and nonlinearly with the intensity of the event, and at the same time the probability of the event drops with its intensity. For this reason, the integral in (1) is usually dominated by costs associated with intensities greater, and possibly much greater, than the intensity associated with the peak of the probability distribution.

This simple point is illustrated in Figure 1 which is based on damage caused to a portfolio of U.S. properties by 6,200 synthetic tropical cyclones making landfall on the U.S. East and Gulf coasts in two different climate states. These tracks were generated using the technique described in Emanuel et al. (2008) applied to a particular CMIP6-generation climate model, and the damage function and portfolio of property values used by Emanuel et al. (2012). The details of the downscaling methodology are described later in this paper but are not so important here; the point is to illustrate the nature of the problem.

The green curves in Figure 1 show the annual probability densities of losses as a function of the loss amount; here these are defined as probabilities per unit base 10 log of the cost. The solid curves are for the climate of the late 20th century, while the dashed curves pertain to the climate of the late 21st century under global warming. The most likely event will incur between $100 thousand and $1 million in losses to this portfolio. The warmer climate has fewer weak events and more strong events; for this illustration the overall frequency is held constant[2]. The violet curves show the probability density multiplied by the cost. The areas under these violet curves are proportional to the total cost. Thus the long-term cost of this hazard is coming from the low-probability, high-intensity tail of the distribution, and the climate shift is causing an appreciable increase in cost even though the shift in the probability distribution is small.

Conversely, *almost no damage is contributed by the median (most frequent)* event. Thus the most frequent question asked by politicians and the media, and many scientists: How will the

[2] The overall frequency includes some events that cause no damage, thus the areas under the probability curves in Fig 1 are not equal.

intensity and frequency of tropical cyclones change? is essentially meaningless, because frequency is dominated by events that cause very little damage. What we must concern ourselves with is the frequency of the most damaging events. While this illustration pertains only to wind damage, the same is qualitatively the case for water damage.

The climate shift in probability density and damage is not simply a matter of changing frequency and/or intensity but also depends crucially on shifting storm tracks; at the end of the day, all meaningful climate change is local. The damage done by a tropical cyclone is also a strong function of its size, including inner dimensions usually characterized by the radius of maximum winds, and the outer wind field. High category tropical cyclones may have radii of maximum winds as small as 10 km and as large as 100 km while their destructiveness varies between the first and second power of this length scale[3]. Moreover, much of the damage done by tropical cyclones is accomplished by water; specifically, by storm surge, which is sensitive to wind speed, storm size, and translation speed, and by torrential rains which are sensitive to a variety of storm structural characteristics, intensity, and movement.

For all these reasons, tropical cyclones simulated by most of today's generation of coupled climate models are unsuitable for direct estimation of tropical cyclone damage. Indeed, the majority of coupled models reviewed by Knutson et al. (2020) have grid spacings of 50 km or greater, whereas numerical convergence experiments (e.g. Rotunno et al. 2009) suggest that

[3] A stationary, steady cyclone just offshore will affect an area proportional the square of its diameter, while a steady storm moving at constant translation speed will affect a swath proportional to the first power of the diameter, but the duration of winds at fixed points will also depend on storm diameter.

grid spacing on the order of a few kilometers is needed to achieve numerical convergence of azimuthal mean variables.

An alternative to using poorly resolved tropical cyclones from climate models is to downscale such models by embedding within them regional or local models with far greater spatial resolution. A straightforward approach is to drive such embedded high-resolution models with time-evolving boundary conditions supplied from the global models. Examples of this approach are comprehensively reviewed in Knutson et al. (2020). A disadvantage of this approach is that the total number of events simulated is limited by the length of time spanned by the global model simulation and/or by computational cost. Furthermore, in designing the geometries of the high-resolution subdomains, one must take into account the possibility that the regions affected by tropical cyclones might shift with climate change.

For this reason, we adapt the approach described in Emanuel et al. (2008) in which the essential statistical properties of the time-evolving environment are culled from global reanalyses or climate models and used to drive a simple coupled ocean-atmosphere tropical cyclone intensity model along tracks produced by random seeding and a beta-and-advection displacement model. The intensity model has very high spatial resolution in the storm core, owing to the use of an angular momentum radial coordinate, and had been previously shown to produce skillful real-time intensity forecasts (Emanuel and Rappaport, 2000). The random seeding is a 'natural selection' algorithm; the vast majority of seed disturbances dissipate quickly owing to having been placed in unfavorable environments, leaving a few survivors that had been placed in favorable environments.

There are several advantages to this technique in comparison to conventional downscaling. The use of angular momentum coordinates allows increasing spatial resolution of the storm core as its intensity increases, thus each storm's intensity is limited by the physical properties of its environment rather than by numerical resolution. Because the tropical cyclone model is driven by the statistics of the global model or reanalysis, an arbitrarily large number of events can be simulated in a given climate, and the seeding is global so there is no need to pre-select sub-domains.

Yet there are a number of disadvantages to this approach. The intensity model is axisymmetric, so the dynamical interaction with sheared environments must be parameterized. The shear parameterization used was developed by Emanuel et al. (2004) to optimize the quality of real-time intensity forecasts and is a function of the 250-850 hPa shear magnitude (but not direction) and the saturation deficit of the large-scale environment at 600 hPa. There is no feedback from the simulated cyclones to the regional environment, as there is in conventional downscaling, so the simulation of the extratropical transition of simulated storms is compromised. (The simulated cyclones do respond to the statistics of middle latitude baroclinic systems but they cannot feedback on such systems.) Finally, in previous work and in what follows here, there has been no attempt to alter the statistics of the random seed disturbances in response to climate change, except that we allow the horizontal scale of the seed disturbances to vary with the deformation radius based on the large-scale environment. Thus we operate under the assumption that the climatology of tropical cyclones is entirely dictated by the large-scale thermodynamic and kinematic environment and not by the climatology of potential initiating disturbances.

Since most tropical cyclones are triggered by pre-existing disturbances, the notion that cyclone climatology is independent of the climatology of such disturbances is counter-intuitive. Yet there is an abundance of evidence that spatial, seasonal, and interannual variability of tropical cyclones is controlled mostly by variations in the large-scale environment. In the first place, genesis potential indices (Gray, 1979; DeMaria et al., 2001; Emanuel and Nolan, 2004; Emanuel, 2010), which are based exclusively on large-scale variables such as potential intensity and wind shear, capture much of the climatology of observed tropical cyclones, including their spatial and seasonal distributions, and interannual variability, at least in the Atlantic region (e.g. Camargo et al., 2007a; Camargo et al., 2007b; Bruyère et al., 2012; Camargo et al., 2014). Classical regional downscaling simulations (e.g. Vitart and co-authors, 2007) for the Atlantic region also capture much of the observed interannual variability of tropical cyclone activity when driven by initial and boundary conditions supplied from reanalysis data, but in this case, potential initiating disturbances such as African Easterly Waves (AEWs) are usually present in the reanalyses and thereby exert an influence on the downscaled tropical cyclones. Yet in one such study (Patricola et al., 2018), AEWs entering the regional domain from the east were artificially suppressed, but the frequency and interannual variability in tropical cyclogenesis was hardly affected. In this case, the AEWs determined the timing and location of genesis events, but not their existence.

The random seeding approach applied here has been shown to capture reasonably well the spatial and seasonal variations of tropical cyclones around the world, and the interannual variability in the Atlantic region, at least as well as classical regional downscaling does (Emanuel et al., 2008). But because the global warming signal is probably not yet detectable in historical

tropical cyclone counts (Knutson et al., 2019), there is no way to definitively test this technique's (or any other's) ability to capture the possibly unique character of the global climate change signal. We will return to this point in Section 4.

2. Methods and Data

We use the same downscaling technique original developed by Emanuel et al. (2006) and Emanuel et al. (2008) and applied to the CMIP5 generation of models by Emanuel (2013). We have made some minor modifications to the technique since its application to CMIP5 models. These include:

- Scaling the radii of maximum winds of the seed disturbances by the deformation radius, based on dry stratification along moist adiabats as determined by the environmental temperature at 600 hPa. This causes a modest increase in the average size of simulated tropical cyclones with warming of the free troposphere.
- Slightly modifying the coefficients governing beta-drift
- Calculating the monthly mean ocean mixed layer depths and sub-mixed layer thermal stratification from the global model output rather than from historical climatology; the effect of this is to modestly reduce the number of very intense storms (Emanuel, 2015)
- Adding detection of secondary eyewalls that occur in the CHIPS model and modifying the canonical radial profiles of wind speed to account for them. This does not affect the global statistics presented here but does affect the calculation of winds speeds at fixed points and thereby, for example, the damage calculations such as those mentioned in the Introduction

- Appling a database of surface roughness over land used to calculate the neutral drag coefficients, replacing the crude parameterization based on topography used before. The new drag coefficients over land are applied to both the CHIPS model and the post-processing algorithms that calculate rainfall. This change does not affect storms over water unless they have previously passed over land.

For the current study, we applied the technique to nine global climate models and to two climate regimes: The period 1850-2014 from historical simulations, and an arbitrary 151-year period from simulations in which atmospheric CO_2 increases by $1\%\ yr^{-1}$. In each case, 150 synthetic tracks were generated for each year, yielding 24,750 events for the historical period, and 22,650 events for the increasing CO_2 simulations. The random seeding rate is calibrated for each model to yield an 1850-2014 average annual global frequency of 84 storms, close to the post-1980 observed mean. The global climate models used are listed in Table 1.

3. Results

We begin by presenting selected time series of global tropical cyclone activity from the historical period, 1850-2014 and from the $1\%\ yr^{-1}$ CO_2 experiment. The latter is carried out over an arbitrary 151-year period, but for purposes of comparison we display the results as extending from 1970 to 2120. But note that the measured rate of increase of atmosphere CO_2 has been closer to $0.2\%\ yr^{-1}$. Our intent here is to examine the general response of global tropical cyclone activity to rising greenhouse gas concentrations, uncomplicated by other climate influences, not to make actual projections. Since the radiative forcing by atmospheric CO_2 over this range of values is nearly proportional to the logarithm of the concentration, we

expect trends in global tropical cyclone activity to scale nearly with the annual percentage increase in CO_2 concentration in the absence of other climate forcings.

In the figures that follow, the solid curves show the multi-model means and the shadings show one standard deviation up and down from the mean. Dashed lines indicate the linear regression trends of the multi-model means. Blue represents the historical period and red shows the $1\%\ yr^{-1}$ CO_2 increase experiment.

Figure 2 shows the annual frequency of all tropical cyclones over the globe. The global frequency increases by about 9% over the historical period, 1850-2014, but more rapidly in the last few decades[4]. Over the 151 years of the increasing CO_2 experiment, the frequency increases by about 25% per doubling of CO_2. Linear trends and associated p-values are given for the annual frequency and other tropical cyclone metrics in Table 2.

The previous downscaling of CMIP5 models yielded an increase of roughly 20% per doubling of CO_2, although those results are not directly comparable to these because the trajectory of CO_2 concentration in the Representative Concentration Pathway (RCP) 8.5 is not the same at that used here.

The green curves in Figure 2 show the values of a genesis potential index (GPI) summed over the globe (weighted by the cosine of the latitude) for each climate model and then averaged to produce the multi-model mean. The GPI is that of Emanuel (2010) except that the absolute

[4] This more rapid increase amounts to around 10 events over the period of good global observations, 1980 – 2018. Given the Poisson random variability of about 9 storms over this period, such a trend would not be statistically detectable at the 5% level, even without considering the effects of natural climate variability on global tropical cyclone frequency.

vorticity contribution is capped at $5\times10^{-5}s^{-1},$ following Tippett et al. (2011). This GPI was developed largely independently of the tropical cyclone downscaling algorithm, so this provides a somewhat independent check, though both the CHIPS model and the GPI use potential intensity and a nondimensional measure of mid-tropospheric specific humidity, $\chi,$ as variables.

Figure 3a shows the multi-model mean global frequency of tropical cyclones categorized by Saffir-Simpson intensity and compares them to observations (IBTrACS, Knapp et al., 2010)[5] made over the period 1980-2018. Note here that the tropical storm (TS) category only includes synthetic and observed events whose lifetime intensity exceeds 40 kts.

The comparison of the observed frequencies with the events downscaled from the historical period is reasonable, but there are too few Category 4 storms and too many Category 5 storms. This may reflect a bias in the downscaling methodology or in the climate models, but it is also likely that the observations, which are overwhelmingly based on satellite remote sensing imagery, underestimate the intensity of the most intense events, shifting them artificially from Category 5 to Category 4 (Kossin et al., 2013). Figure 3b shows the same comparison but increasing the intensities of the observed storms by 10%. This increase brings the observed and historically simulated Saffir-Simpson categories into much better alignment, though the partitioning between tropical storms and Category 1 storms deteriorates, perhaps because of the ambiguity of Dvorak method when eyes are beginning to form (Olander and Velden, 2019). The observed and historically simulated combined numbers of tropical storms and Category 1

[5] Data for the North Atlantic and eastern and Central North Pacific originated from the National Oceanographic and Atmospheric Administration's National Hurricane Center, and elsewhere from the U.S. Navy's Joint Typhoon Warning Center.

214 storms are in very good agreement. Thus it is likely that either the actual storm intensities are
215 underestimated or the simulated storm intensities are overestimated. We note that the 10%
216 adjustment does not improve the agreement in the Atlantic region (not shown), perhaps
217 because storms are better observed there. CO_2–induced warming brings about increases in the
218 frequency of all categories, but the increases in Category 2 and 3 events are small. These are in
219 a flat minimum in the frequency distribution among categories, so that a shift to higher
220 intensities at constant overall frequency would lead to little change in the frequencies of those
221 categories.

222 Figure 4 is in the same format as Figure 2, but shows the evolution over time of the power
223 dissipation index, which is the sum over each track and over all tracks in a given year of the
224 cube of the maximum surface wind. The power dissipation increases at a rate of about 30% per
225 doubling of CO_2. This is lower than the CMIP5 result (Emanuel, 2013) of closer to 40%. Note
226 also, from Table 2, the statistically significant increase of about 15% through the period 1850-
227 2014.

228 We also consider a landfall power dissipation index, which is the cube of the wind speed at
229 landfall summed over all landfalling events in each year. Here landfall is determined using a ¼ x
230 ¼ degree bathymetry/topography data set, and we consider all landfalls, even if a storm makes
231 landfall more than once. Figure 5 and Table 2 show that the multi-model mean landfall power
232 dissipation increases by about 9% over the historical period and the projected increase is about
233 25% per doubling of CO_2, a bit less than the open-ocean increase in power dissipation.

234 The spatial patterns of three multi-model mean tropical cyclone metrics and their changes with
235 increasing CO_2 are shown in Figure 6. The top row shows genesis density – the number of
236 genesis events per 1-degree latitude square per year – while the middle row shows the track
237 density and the bottom row shows the power dissipation density. In the case of track density,
238 each track is counted only once in any lat-long box used to grid the data, whereas the power
239 dissipation is summed over all 2-hour points along each track in each box. The left side of Figure
240 6 is based on IBTrACS data from 1979-2015 while the middle column shows multi-model mean
241 quantities from the historical downscaling. The right-hand side of figure 6 shows the
242 percentage change between the mean over this historical period and the mean over the
243 $1\%\, yr^{-1}$ increasing CO_2 simulations. The change is displayed only where at least 7 of the 9
244 models agree with each other on the sign of the change.

245 The historical mean fields in Figure 6 shows some of the same biases noted in the CMIP5
246 downscaling and also present in the climatologies of storms explicitly simulated in many of
247 these models (e.g. Camargo, 2013) and in CMIP6 models (Roberts et al., 2020). There are too
248 many storms in the southern hemisphere, including the South Atlantic, and too few tropical
249 cyclones in the eastern North Pacific. Genesis is too active in the central North Pacific, and
250 there are too few storms in the North Atlantic. Some of these biases are also present in tropical
251 cyclones downscaled from climate reanalyses (not shown), so these are probably an artifact of
252 the downscaling technique. It is evident from the track density maps that the downscaled
253 tracks extend somewhat further poleward than the IBTrACS storm tracks, except in the North
254 Atlantic. This is likely owing to differing conventions on when to terminate tracks of tropical
255 cyclones undergoing extratropical transition. Most forecasting agencies terminate tropical

cyclone tracks when the storm is deemed to have become mostly extratropical. Termination of the downscaled tracks, on the other hand, is based only on the intensity having fallen below a set threshold. Thus we expect that downscaled extratropical transitioning storms will be carried somewhat further poleward than IBTrACS events.

Turning attention to the percentage changes between the historical to the global warming simulations (right-hand column of Figure 6), note that there is essentially no change in any metric in the South Pacific, as was the case in downscaling the CMIP5 models. There is little change in the genesis rate in the South Indian Ocean, but the power dissipation increases and the tracks extend somewhat further poleward, suggesting that the tropical cyclones in this part of the world become more intense and are able to travel further poleward before dissipating.

The most profound changes occur in the northern hemisphere. The genesis maps show a northward expansion of the North Atlantic genesis region and the central and western North Pacific genesis belts. The eastern North Pacific and Arabian Sea genesis regions both expand westward. Partially as a result of these changes in genesis, there are large increases in track density and power dissipation throughout much of the northern hemisphere, especially in the central North Pacific and the subtropical to high latitude North Atlantic. The largest percentage increases are, fortunately, away from land. Especially noteworthy is the large increase in track density in the high latitudes of the North Atlantic, suggesting that the northward expansion of the Atlantic genesis region and the increase in storm intensity there lead to a greater incidence of extratropical transition. This is consistent with recent projections of extratropical transition

276 that suggest increases in the western North Pacific and North Atlantic (Liu et al., 2017;
277 Michaelis and Lackmann, 2019).

278 The large increase in tropical cyclone activity in the northern hemisphere relative to the
279 southern hemisphere is consistent with explicitly simulated storms in CMIP6 models (Roberts et
280 al., 2020) and the pattern of changes in track density resembles both observed changes over
281 the period 1980-2018 and changes simulated by a suite of high-resolution coupled models over
282 the same period (Murakami et al., 2020), with large increases in the North Atlantic and central
283 North Pacific. But the same models, forced by increasing CO_2 alone, show decreasing track
284 density in the North Atlantic.

285 The poleward expansion of both the track and power dissipation density in the northern
286 hemisphere and South Indian Ocean is consistent with recent observations of the poleward
287 migration of the latitudes at which tropical cyclones are observed to reach peak intensity
288 (Kossin et al., 2014) and with projected poleward migration in the western North Pacific (Kossin
289 et al., 2016).

290 In forecasting individual tropical storms, the intensification rate is an important consideration
291 because rapidly intensifying events near the time of landfall can catch forecasters and
292 emergency managers off guard. Theoretically, intensification rates should scale as the square of
293 the potential intensity, so they are more sensitive to climate change than the intensity itself
294 (Emanuel, 2017). Figure 7a shows the base 10 logarithm of the probability densities of the
295 multi-model mean and standard deviation of intensification rates based on two-hourly fixes of
296 the downscaled tropical cyclones. These probability densities are independent of overall storm

297 frequency. Figure 7b shows the percentage difference between the historical period and the
298 $1\%\ yr^{-1}$ simulations. There are large percentage increases in intensification rates exceeding
299 about $3\,kts\,hr^{-1}$, and this percentage change increases with intensification rate. There is also a
300 smaller increase in extreme dissipation rates, likely owing to the faster decay rates of initially
301 more intense storms over land and cold water, because the decay rates scale roughly with the
302 square of the surface wind speed.

303 The flooding potential, and to some extent the wind damage, caused by tropical cyclones can
304 be strongly affected by their translation speed. Slower moving storms will affect a given region
305 for a longer period, producing more rain and perhaps more wind damage. On the other hand,
306 slow-moving storms are not likely to travel as far inland, sparing regions away from coastlines.

307 Figure 8 shows the multi-model average translation speed of downscaled tropical cyclones for
308 the historical period (a) and the change in translation speed (b) for a transient doubling of CO_2.
309 The latter is displayed only where at least 7 of the 9 GCMs agree on the sign of the change in
310 downscaled translation speed. Remarkably, there is no significant change in translation speed in
311 the deep tropics, but there is a substantial decrease in mean translation speed at the
312 subtropical peripheries of the tropical belt, affecting the U.S. east and Gulf coasts, the central
313 coast of China, Korea, southern Japan, and Australia. This is perhaps a consequence of the
314 projected poleward expansion of the Hadley circulation. This result can be compared and
315 contrasted to recent global modeling results that show , reductions in the subtropics and
316 middle and high latitudes (Yamaguchi et al., 2020), and reductions primarily in middle latitudes

(Zhang et al., 2020). Lee et al. (2020) used a downscaling method similar to that employed here to examine translations speeds of storms near land, finding a slight reduction.

4. Discussion

a. Changes in weak tropical cyclones

As was the case with downscaling the previous (CMIP5) generation of climate models, the results of downscaling nine CMIP6 models show substantial increases in both the intensity and frequency of tropical cyclones as greenhouse gas concentrations increase. The frequency increase is at odds with most (though not all) results from explicit modeling of tropical cyclones. According to a recent and comprehensive review by Knutson et al. (2020), "the vast majority of individual studies (22 out of 27 studies) project a decrease in global TC frequency with greenhouse warming." It is both of inherent and practical interest to discover why these results differ the way they do.

It should first be noted that the great majority of the studies done to date focused on tropical cyclones explicitly simulated in global atmospheric or coupled general circulation models (GCMs), whose effective horizontal grid spacings varies from 14 km to as much as 200 km. Most of these models moderately to severely under-resolve tropical cyclones (e.g. see Rotunno et al., 2009) and the mesoscale processes observed to be involved in their genesis (e.g. Montgomery and Smith, 2012). Tropical cyclones that develop in such models must be detected using an algorithm (e.g. Walsh et al., 2007) and the counts of tropical cyclones are known to be sensitive to how that algorithm is formulated and to model characteristics (Raavi and Walsh, 2020).

In particular, climate change may alter the scale and other characteristics of simulated tropical cyclones, pushing events across arbitrary detection thresholds and thereby leading to false trends in counts of weak events. For example, weak tropical cyclone-like disturbances may become broader as the climate warms, as they do in "TC-world" experiments (e.g. Khairoutdinov and Emanuel, 2013), and while their circulation may stay the same or even increase, their vorticity may decrease below the imposed vorticity thresholds that are a key feature of most tropical cyclone detection algorithms. Indeed, in their analysis of 850 hPa vorticity in two global models, Sugi et al. (2020) show that as climate warms, the vorticity of disturbances of tropical storm strength decreases proportionally more than does their intensity (compare their figures 2 and 3), suggesting that the pre-tropical cyclone disturbances may be becoming broader.

To test the idea that this could bias trends in explicitly detected cyclones in GCMs, we re-calculated time series of downscaled tropical cyclone metrics as before but this time imposing an artificial vorticity-like detection threshold. Specifically, we discarded events whose ratio of maximum circular wind speed to radius of maximum winds is less than $6 \times 10^{-4} s^{-1}$.

Figure 9 compares the evolution of total tropical cyclone frequency in this modified experiment to the control, for both the historical and increasing CO_2 simulations of one of the 9 models we use in this study. The substantial upward trend of the control frequency in this latter simulation is greatly muted in the modified experiment. In both the control and the modified experiments, the horizontal scale of the seed disturbances is determined by the local deformation radius,

which increases as the climate warms owing to the increase in dry static stability along moist adiabats.

Thus it is possible that the frequency of disturbances detected by a vorticity threshold may decrease relative to the frequency determined by a wind speed threshold. Almost all the GCM-based studies reviewed by Knutson et al. (2020) imposed both vorticity and wind speed detection thresholds, so further research would be necessary to confirm or reject the hypothesis that warming-induced trends in tropical cyclone counts may be negatively biased through the use of a fixed vorticity threshold that does not depend on the climate state.

There are also indications that explicitly simulated tropical cyclones and their sensitivity to climate change may not be robust to changes in model physics or resolution. For example, when the grid spacing of a coupled global climate model was decreased from 50 km to 25 km, the sensitivity of tropical cyclone counts to global warming went from negative to neutral (Vecchi et al., 2019). Moreover, in contrast to both observations (Tippett et al., 2011) and the downscaling described here, the relationship between explicit tropical cyclone counts in GCMs and environmental conditions is weak and/or of the wrong character (Camargo et al., 2020).

For these reasons, there is little basis for confidence in the projection by most climate models that overall tropical cyclone frequency will decline. Indeed, 7 of the 11 authors of Knutson et al. (2020) rated confidence in the projection of decreasing tropical cyclone frequency as low-to-medium.

But how believable are the indications of increasing frequency across the spectrum of intensity resulting from this downscaling study (see Figure 3)? On the one hand, there is excellent correspondence between the downscaled tropical cyclone frequency and the genesis potential index calculated from the raw GCM output (Figure 2). The GPI was developed and tested largely independently of the development of the downscaling technique, though the variables used in the GPI were selected partly because they are variables that appear naturally in the CHIPS model[6]: Both the CHIPS model and the GPI depend strongly on potential intensity, wind shear, and the mid-tropospheric dryness parameter χ that is based on moist static energy. There is no a priori reason to think that variations in these parameters owing to global climate change would affect tropical cyclones differently from variations owing to spatial, annual and interannual variability, yet both the downscaling and the GPI capture such natural variations quite well. There are, of course, other empirically determined genesis potential indices (e.g. (Tippett et al., 2011; Tang and Camargo, 2014) and given that these produce different estimates, agreement with the downscaled frequencies presented here would likely be less.

By examining each of the factors that make up the definition of GPI, it is possible to draw some inferences about which environmental factors lead to its increase. The definition of GPI used here is from Emanuel (2010):

$$GPI \equiv |\eta|^3 \, \chi^{-4/3} MAX\left(\left(V_{pot} - 35\, ms^{-1}\right), 0\right)^2 \times \left(25\, ms^{-1} + V_{shear}\right)^{-4}, \quad (2)$$

[6] This GPI is also dimensionally correct, yielding genesis number per unit area per unit time. Other genesis indices perform equally well during the historical period but yield very different trends in global warming scenarios (Lee et al., 2020).

where η is the absolute vorticity of the 850 hPa flow, capped by $5\times$, V_{pot} is the potential intensity, V_{shear} is the magnitude of the 850 hPa-250 hPa wind shear, and

$$\chi \equiv \frac{s_b - s_m}{s_0^* - s_b}, \tag{3}$$

where s_b , s_m , and s_0^* are the moist entropies of the boundary layer and middle troposphere, and the saturation moist entropy of the sea surface, respectively. This is the quantity that is summed over the globe and averaged among the 9 models to produce the green curves in Figure 2. Were it not for that summation, it would be possible to fo a linear factor separation of (2) by taking the logarithm of both sides:

$$\log(GPI) = 3\log(|\eta|) - \frac{4}{3}\log(\chi) + 2\log\left(MAX\left(\left(V_{pot} - 35\ ms^{-1}\right),1\right)\right) - 4\log\left(25\ ms^{-1} + V_{shear}\right). \tag{4}$$

Unfortunately, the summation over the globe and the averaging among the 9 models does not allow this: The logarithm of the summed, averaged value of GPI given by (2) is not equal to the summed, averaged value of the logarithm of GPI. Since the tuning of the coefficients in (2) was done by matching summed GPI to observations, one cannot willy-nilly use (4) instead of (3) as the working definition of the GPI without re-turning. Since that re-tuning is beyond the scope of this study, we attempt to use (4) anyway, using the summed, averaged quantities (GPI, η etc.) before taking their logarithms.

Figure 10 shows, for the 1% per year increasing CO_2 experiment, the evolution with time of the terms in (4), where it is understood that the quantities have first been summed and then averaged among the 4 models. To avoid extratropical influences, we zero each individual term

wherever the potential intensity is $35\ ms^{-}$ or less, and each curve is relative to the initial value of the quantity in question.

The black curve shows the sum of the terms whereas the green curve is the logarithm of the actual GPI; the mismatch between these two curves reflects the problems alluded to above. But for what it is worth, one sees that the potential intensity and saturation deficit are the dominant terms and work in opposing directions. The negative contribution of the saturation deficit χ is consistent with the results of Emanuel et al. (2008) and Lee et al. (2020) and suggest that the main break on increasing tropical cyclone frequency in a warming climate is the increasing saturation deficit of the middle troposphere. The vorticity and shear contributions are smaller, but both terms act to increase the GPI trend.

To the extent that the GPI reflects the physics of the downscaled tropical cyclones, we would infer that increasing potential intensity is the most important contributor to increasing cyclone frequency, with small additional contributions from decreasing shear and increasing vorticity (likely reflecting the poleward migration of genesis regions). Increasing saturation deficit works in the opposite direction, acting to decrease storm frequency.

It should be noted, however, that changing the exponent of χ in (2) to -2 changes the sign of the net response of the GPI to increasing CO_2 concentration while not strongly degrading the fit to observed variability, so the good fit to the downscaled frequencies is somewhat coincidental. Thus the agreement between the downscaled frequencies and the GPI should not be interpreted as strong evidence for the correctness of either.

Returning to the downscaled tropical cyclones, their rate of genesis varies directly with the specified seeding rate, which is held constant across the globe, seasonally, interannually, and with global climate change. Arguments have been made that this seeding rate should decline as the globe warms (Sugi et al., 2020). Yet the strong spatial, seasonal and interannual variation of potential initiating disturbances in the current climate does not seem to preclude the ability of either the GPI or the downscaling from capturing major features of natural tropical cyclone variability (Camargo et al., 2007a; Emanuel et al., 2008). Moreover, Patricola et al. (2018) showed that suppressing African easterly waves, a prominent catalyst for North Atlantic hurricanes, did not change the level of tropical cyclone activity in a regional tropical North Atlantic model, though the waves did determine the location and timing of genesis events. Thus the seed disturbances, in this case, did not control the level of tropical cyclone activity.

A more serious deficiency of the downscaling method applied here is that there is no feedback whatsoever between the downscaled tropical cyclones and the large-scale environment that is driving them. Even regional downscaling models, such as that used by Patricola et al. (2018), can simulate some regional feedbacks of cyclone activity within the regional model itself, though they cannot influence the global model in which the regional model is embedded.

There are two known feedback mechanisms by which current tropical cyclone activity can potentially influence future activity though modification of their large scale environment. The first acts primarily though the ocean: Tropical cyclones cool the sea surface by mixing warmer surface waters with cooler water below the mixed layer (Leipper, 1967; Price, 1981) and subsequent re-heating of the cold wakes leads to a net export of heat away from the affected

region (Emanuel, 2001; Federov et al., 2010). This has the negative feedback of cooling the ocean in tropical cyclone regions, reducing the genesis potential there, but it may lead to increases in genesis in marginal regions outside the main tropical cyclone belts.

A second negative feedback acts through the atmosphere: It is the profound drying of the atmosphere that occurs with any form of aggregation of convection (Bretherton and Khairoutdinov, 2004; Wing et al., 2017). This will greatly increase the inhibition to tropical cyclogenesis represented in the GPI by the χ parameter and known to strongly affect the genesis rates in the downscaling technique applied here (Emanuel et al., 2008).

Both these mechanisms are, in principle, operating in fully coupled GCMs. To the extent that the large-scale fields are affected by these feedbacks in the GCMs used here, they will also decrease the number of downscaled genesis events, but owing to the severe under-resolution of tropical cyclones in most GCMs, these negative feedbacks may be strongly muted.

But there are now some global coupled models with resolutions high enough to capture most of the full spectrum of tropical cyclone numbers and intensities. One such model, the Model for Prediction Across Scales–Atmosphere (MPAS-A), which was emplyed by Michaelis and Lackmann (2019) to make global projections of the response of tropical cyclone activity to global warming using a 15-km grid over the whole of the northern hemisphere. Notably, they used a cyclone detection algorithm based on sea level pressure anomalies with no vorticity threshold. They found increasing tropical cyclone frequency in the northern hemisphere, especially in the Atlantic.

475 Another high-resolution global coupled model is the NOAA Geophysical Fluid Dynamics high
476 atmospheric resolution version of the Forecast-oriented Low Ocean Resolution version of the
477 GFDL global climate model (HiFLOR; Murakami et al., 2015). With an effective grid spacing of
478 about 25 km, this model explicitly simulates high intensity tropical cyclones (Vecchi et al.,
479 2019). Climate sensitivity experiments with HiFLOR show that increasing CO_2 concentrations
480 leads to a statistically insignificant change in global tropical cyclone counts but a substantial
481 increase in high intensity events (Vecchi et al., 2019). We downscaled 200 events globally per
482 year for 200 years of simulation in two different climates: the climate of the late 20th century
483 and a climate representing increased CO_2 concentrations. In the former, a single year
484 representing atmospheric greenhouse and aerosol conditions in the year 1990 was repeated
485 over 300 years; we used the last 200 years in the downscaling. The warming experiment starts
486 at year 100 of the control simulation and increases CO_2 at the rate of 1% per year until a
487 doubling has been reached after 70 years; thereafter the CO_2 concentration remains fixed for
488 another 230 years. We use the last 200 years of this simulation. Details may be found in Irvine
489 et al. (2019).

490 Figure 11 shows changes in global counts of tropical cyclones in each Saffir-Simpson category.
491 Note that the HiFLOR model produces about 90 tropical storms per year globally, close to the
492 observed frequency, while the downscaled results have been calibrated to an annual frequency
493 of 84 events in the 20th century. The distribution across categories of the response of the
494 downscaled tropical cyclones to doubling CO_2 is consistent with that resulting from downscaling
495 of the CMIP6 models (see Figure 2) but substantially muted in comparison. At the same time,
496 there are substantial increases in the explicitly simulated high intensity (Cat 4-5) tropical

cyclones in HiFLOR, while the number of weak events (tropical storms and CAT1 hurricanes) decreases. We speculate that the increase in explicitly simulated intense storm activity in HiFLOR may have led to the aforementioned negative feedbacks, which muted the response of the downscaled storms.

In the author's opinion, the limitations of CMIP6 model simulations of tropical cyclones preclude any robust projection of the response of weak tropical cyclone activity to global warming, either from their explicitly simulated storms or from events downscaled from their output.

b. Changes in high intensity tropical cyclones

In contrast to the case of marginal storms, detection of cyclones in GCMs becomes less of an issue for intense storms, particularly in the case of high resolution models that can simulate the full intensity spectrum. Perhaps for this reason, there is much better agreement on projected changes in intense (Category 4-5) tropical cyclones, both among the explicitly simulated storms and between them and the downscaled storms (see Figure 2c and compare to Figure 2a of Knutson et al. 2020).

5. Summary

The application of a downscaling technique to 9 CMIP6-generation climate models suggests potentially large increases in various measures of tropical cyclone activity in response to anthropogenic climate change, particularly in the northern hemisphere. These results are broadly consistent with those from downscaling CMIP5 models (Emanuel, 2013).

As reviewed by Knutson et al. (2020), there is a moderately strong consensus on an increase in high intensity tropical cyclones and in tropical cyclone rainfall. There is little agreement on how the frequency of weak storms might change, but with the possible exception of rainfall, these are of little consequence. The fact that most explicit modeling studies agree that tropical cyclone frequency will decrease with climate warming may be an artifact of low resolution and the use of non-climate-dependent detection thresholds. Their agreement with each other is only prima facie evidence of robustness of the trend. In the author's opinion, though, the increases in overall tropical cyclone frequency predicted by our downscaling would be muted and perhaps even eliminated by feedbacks from the cyclones to their large-scale environment in two-way coupled simulations that adequately resolve tropical cyclones.

The large increase in the probability of rapid intensification rates is perhaps one of the more worrying aspects of the effect of climate change on tropical cyclones. Given the level of uncertainty in contemporary tropical cyclone intensity forecasts, increasing rates of intensification increase the chances of surprises (Emanuel, 2017).

Consistent with some observational studies (Kossin, 2018), there is a robust projected decrease in tropical cyclone translation speed in the subtropics, though not in the deep tropics. This may increase the probability of stalling storms, such as Harvey of 2017 and Dorian of 2019. These storms can be especially destructive because of prolonged rain and/or wind.

While the jury may still be out on the effects of climate change on the incidence of weak storms, the growing consensus on substantial increases in high-intensity storms and rainfall paints a robust picture of increasing tropical cyclone risk as the climate continues to warm.

Acknowledgements: The author is grateful for the support from the National Science Foundation under grant ICER-1854929. CMIP6 climate model data was downloaded from a website operated by the Earth System Grid Federation.

Data availability statement: The downscaled tropical cyclone data used in this study is freely available from the author for research purposes only. Recipients will be asked to sign and return a data non-redistribution agreement.

References

Bretherton, C. S., and M. F. Khairoutdinov, 2004: Convective self-aggregation in large cloud-resolving model simulations of radiative convective equilibrium. *AMS Conference on Hurricanes and Tropical Meteorology*, Miami, Amer. Meteor. Soc.,

Bruyère, C. L., G. J. Holland, and E. Towler, 2012: Investigating the use of a genesis potential index for tropical cyclones in the North Atlantic basin. *J. Climate*, **25,** 8611-8626, doi:10.1175/jcli-d-11-00619.1.

Camargo, S., 2013: Global and regional aspects of tropical cyclone activity in the CMIP5 models. *J. Climate*, **26,** 9880–9902.

Camargo, S. J., K. A. Emanuel, and A. H. Sobel, 2007a: Use of a genesis potential index to diagnose ENSO effects on tropical cyclone genesis. *J. Climate*, **20,** 4819-4834, doi:10.1175/Jcli4282.1.

Camargo, S. J., A. H. Sobel, A. G. Barnston, and K. A. Emanuel 2007b: Tropical cyclone genesis potential index in climate models. *Tellus A*, **59,** 428-443, doi:10.1111/j.1600-0870.2007.00238.x.

Camargo, S. J., M. K. Tippett, A. H. Sobel, G. A. Vecchi, and M. Zhao, 2014: Testing the performance of tropical cyclone genesis indices in future climates using the HIRAM model. *J. Climate*, **27,** 9171-9196, doi:10.1175/jcli-d-13-00505.1.

Camargo, S. J., and co-authors, 2020: Characteristics of model tropical cyclone climatology and the large-scale environment. *J. Climate*, **33,** 4463-4487, doi:10.1175/jcli-d-19-0500.1.

566 Danabasoglu, G., and Coauthors, 2020: The community earth system model version 2 (CESM2).
567 *JAMES*, **12,** e2019MS001916, doi:10.1029/2019ms001916.

568 DeMaria, M., J. A. Knaff, and B. H. Connell, 2001: A tropical cyclone genesis parameter for the
569 tropical Atlantic. *Wea. Forecast.***,** 219-233.

570 Emanuel, K., and E. Rappaport, 2000: Forecast skill of a simplified hurricane intensity prediction
571 model. *Preprints of the 24th Conf. Hurricanes and Trop. Meteor.*, Ft. Lauderdale, FL,
572 Amer. Meteor. Soc., Boston, 236-237,

573 Emanuel, K., C. DesAutels, C. Holloway, and R. Korty, 2004: Environmental control of tropical
574 cyclone intensity. *J. Atmos. Sci.*, **61,** 843-858.

575 Emanuel, K., and D. Nolan, 2004: Tropical cyclone activity and global climate. *26th Conference*
576 *on Hurricanes and Tropical Meteorology*, Miami, Amer. Meteor. Soc., 240-241,

577 Emanuel, K., R. Sundararajan, and J. Williams, 2008: Hurricanes and global warming: Results
578 from downscaling IPCC AR4 simulations. *Bull. Amer. Meteor. Soc.*, **89,** 347-367.

579 Emanuel, K., 2010: Tropical cyclone activity downscaled from NOAA-CIRES reanalysis, 1908-
580 1958. *J. Adv. Model. Earth Sys.*, **2,** 1-12.

581 Emanuel, K., F. Fondriest, and J. Kossin, 2012: Potential economic value of seasonal hurricane
582 forecasts. *Weather, Climate, and Society*, **4,** 110-117, doi:10.1175/wcas-d-11-00017.1.

583

584 Emanuel, K., 2013: Downscaling CMIP5 climate models shows increased tropical cyclone activity
585 over the 21st century. *Proc. Nat. Acad. Sci.*, **110,** 12219–12224,
586 doi:/10.1073/pnas.1301293110.

587 ——, 2015: Effect of upper-ocean evolution on projected trends in tropical cyclone activity. *J.*
588 *Climate*, **28,** 8165-8170.

589 ——, 2017: Will global warming make hurricane forecasting more difficult? . *Bull. Amer.*
590 *Meteor. Soc.*, **98,** 495-501.

591 Emanuel, K. A., 2001: The contribution of tropical cyclones to the oceans' meridional heat
592 transport. *J. Geophys. Res.*, **106,** 14,771-714,782.

593 Emanuel, K. A., S. Ravela, E. Vivant, and C. Risi, 2006: A statistical-deterministic approach to
594 hurricane risk assessment. *Bull. Amer. Meteor. Soc.*, **19,** 299-314.

595 Federov, A. V., C. M. Brierley, and K. Emanuel, 2010: Tropical cyclones and permanent El Niño in
596 the early Pliocene epoch. *Nature*, **463,** 1066-1070.

597 Gaul, G. M., 2019: *The geography of risk: Epic storms, rising seas, and the cost of America's*
598 *coasts.* Farrar, Straus and Giroux, New York, 304 pp., translator, 9780374160807.

599 Gray, W. M., 1979: Hurricanes: Their formation, structure, and likely role in the tropical
600 circulation. *Meteorology over the tropical oceans*, D. B. Shaw, Ed., Roy. Meteor. Soc.,
601 155-218 pp.

602

603 Hourdin, F., and Coauthors, 2016: Lmdz6a: The atmospheric component of the IPSL climate
604 model with improved and better tuned physics. *JAMES*, **n/a,** e2019MS001892,
605 doi:10.1029/2019ms001892.

606 Irvine, P., K. Emanuel, J. He, L. W. Horowitz, G. Vecchi, and D. Keith, 2019: Halving warming with
607 idealized solar geoengineering moderates key climate hazards. *Nat Clim Change*, **9,** 295-
608 299, doi:10.1038/s41558-019-0398-8.

609 Khairoutdinov, M. F., and K. Emanuel, 2013: Rotating radiative-convective equilibrium
610 simulated by a cloud-resolving model. *J. Adv. Model. Earth Sys.*, **5,** 816-825,
611 doi::10.1002/2013MS000253.

612 Knapp, K. R., M. C. Kruk, D. H. Levinson, H. J. Diamond, and C. J. Neumann, 2010: The
613 international best track archive for climate stewardship (IBTrACS). *Bull. Amer. Meteor.*
614 *Soc.*, **91,** 363-376, doi:10.1175/2009bams2755.1.

615 Knutson, T., and Coauthors, 2019: Tropical cyclones and climate change assessment: Part I:
616 Detection and attribution. *Bull. Amer. Meteor. Soc.*, **100,** 1987-2007, doi:10.1175/bams-
617 d-18-0189.1.

618 ——, 2020: Tropical cyclones and climate change assessment: Part II: Projected response to
619 anthropogenic warming. *Bull. Amer. Meteor. Soc.*, **101,** E303-E322, doi:10.1175/bams-d-
620 18-0194.1.

621 Kossin, J. P., T. L. Olander, and K. R. Knapp, 2013: Trend analysis with a new global record of
622 tropical cyclone intensity. *J. Climate*, **26,** 9960-9976, doi:10.1175/jcli-d-13-00262.1.

623 Kossin, J. P., K. A. Emanuel, and G. A. Vecchi, 2014: The poleward migration of the location of
624 tropical cyclone maximum intensity. *Nature*, **509,** 349, doi:10.1038/nature13278.

625 Kossin, J. P., K. A. Emanuel, and S. J. Camargo, 2016: Past and projected changes in western
626 North Pacific tropical cyclone exposure. *J. Climate*, **29,** 5725-5739, doi:10.1175/jcli-d-16-
627 0076.1.

628 Kossin, J. P., 2018: A global slowdown of tropical-cyclone translation speed. *Nature*, **558,** 104-
629 107, doi:10.1038/s41586-018-0158-3.

630 Lee, C.-Y., S. J. Camargo, A. H. Sobel, and M. K. Tippett, 2020: Statistical–dynamical downscaling
631 projections of tropical cyclone activity in a warming climate: Two diverging genesis
632 scenarios. *J. Climate*, **33,** 4815-4834, doi:10.1175/jcli-d-19-0452.1.

633 Leipper, D. F., 1967: Observed ocean conditions and Hurricane Hilda, 1964. *J. Atmos. Sci.*, **24,**
634 182-196.

635 Liu, M., G. A. Vecchi, J. A. Smith, and H. Murakami, 2017: The present-day simulation and
636 twenty-first-century projection of the climatology of extratropical transition in the North
637 Atlantic. *J. Climate*, **30,** 2739-2756, doi:10.1175/jcli-d-16-0352.1.

638 Michaelis, A. C., and G. M. Lackmann, 2019: Climatological changes in the extratropical
639 transition of tropical cyclones in high-resolution global simulations. *J. Climate*, **32,** 8733-
640 8753, doi:10.1175/jcli-d-19-0259.1.

641

642 Montgomery, M. T., and R. K. Smith, 2012: The genesis of Typhoon Nuri as observed during the
643 tropical cyclone structure 2008 (TCS08) field experiment. Part 2: Observations of the
644 convective environment. *Atmos. Chem. Phys.*, **12,** 4001-4009, doi:10.5194/acp-12-4001-
645 2012.

646 Müller, W. A., and Coauthors, 2018: A higher-resolution version of the Max Planck Institute
647 earth system model (mpi-esm1.2-hr). *JAMES*, **10,** 1383-1413,
648 doi:10.1029/2017ms001217.

649 Murakami, H., and Coauthors, 2015: Simulation and prediction of category 4 and 5 hurricanes in
650 the high-resolution GFDL HiFLOR coupled climate model. *J. Climate*, **28,** 9058-9079,
651 doi:10.1175/jcli-d-15-0216.1.

652 Murakami, H., T. L. Delworth, W. F. Cooke, M. Zhao, B. Xiang, and P.-C. Hsu, 2020: Detected
653 climatic change in global distribution of tropical cyclones. *Proc. Nat. Acad. Sci.*, **117,**
654 10706-10714, doi:10.1073/pnas.1922500117.

655 Olander, T. L., and C. S. Velden, 2019: The advanced Dvorak technique (ADT) for estimating
656 tropical cyclone intensity: Update and new capabilities. *Wea. Forecast.*, **34,** 905-922,
657 doi:10.1175/waf-d-19-0007.1.

658 Patricola, C. M., R. Saravanan, and P. Chang, 2018: The response of Atlantic tropical cyclones to
659 suppression of African easterly waves. *Geophys. Res. Lett.*, **45,** 471-479,
660 doi::10.1002/2017GL076081.

661 Price, J. F., 1981: Upper ocean response to a hurricane. *J. Phys. Ocean.*, **11,** 153-175, doi:
662 10.1175/1520-0485.

663 Raavi, P. H., and K. J. E. Walsh, 2020: Sensitivity of tropical cyclone formation to resolution-
664 dependent and independent tracking schemes in high-resolution climate model
665 simulations. *Earth and Space Science*, **7,** e2019EA000906, doi:10.1029/2019ea000906.

666 Roberts, M. J., and Coauthors, 2020: Projected future changes in tropical cyclones using the
667 CMIP6 HighResMIP multi-model ensemble. *Geophys. Res. Lett.*, **n/a,** e2020GL088662,
668 doi:10.1029/2020gl088662.

669 Rotunno, R., Y. Chen, W. Wang, C. Davis, J. Dudhia, and C. L. Holland, 2009: Large-eddy
670 simulation of an idealized tropical cyclone. *Bull. Amer. Meteor. Soc.*, **90,** 1783-1788.

671 Sellar, A. A., and Coauthors, 2020: Implementation of U.K. Earth system models for CMIP6.
672 *JAMES*, **12,** e2019MS001946, doi:10.1029/2019ms001946.

673 Sugi, M., Y. Yamada, K. Yoshida, R. Mizuta, M. Nakano, C. Kodama, and M. Satoh, 2020: Future
674 changes in the global frequency of tropical cyclone seeds. *SOLA*, **16,** 70-74,
675 doi:10.2151/sola.2020-012.

676 Swart, N. C., and Coauthors, 2019: The Canadian earth system model version 5 (CANESM5.0.3).
677 *Geosci. Model Dev.*, **12,** 4823-4873, doi:10.5194/gmd-12-4823-2019.

678 Tang, B., and S. J. Camargo, 2014: Environmental control of tropical cyclones in CMIP5: A
679 ventilation perspective. *JAMES*, **6,** 115-128, doi:10.1002/2013ms000294.

680 Tatebe, H., and Coauthors, 2019: Description and basic evaluation of simulated mean state,
681 internal variability, and climate sensitivity in MIROC6. *Geoscientific Model Development*,
682 **12,** 2727-2765, doi:10.5194/gmd-12-2727-2019.

683 Tippett, M. K., S. Camargo, and A. H. Sobel, 2011: A Poisson regression index for tropical
684 cyclone genesis and the role of large-scale vorticity in genesis. *J. Climate*, **24,** 2335-2357.

685 Vecchi, G. A., and Coauthors, 2019: Tropical cyclone sensitivities to CO2 doubling: Roles of
686 atmospheric resolution, synoptic variability and background climate changes. *Clim. Dyn.*,
687 **53,** 5999-6033, doi:10.1007/s00382-019-04913-y.

688 Vitart, and co-authors, 2007: Dynamically-based seasonal forecasts of Atlantic tropical storm
689 activity issued in june by eurosip. *Geophys. Res. Lett ,*, **34,** L16815.

690 Voldoire, A., and Coauthors, 2019: Evaluation of CMIP6 deck experiments with CNRM-cm6-1.
691 *JAMES*, **11,** 2177-2213, doi:10.1029/2019ms001683.

692 Walsh, K., M. Fiorino, C. W. Landsea, and K. L. McInnes, 2007: Objectively determined
693 resolution-dependent threshold criteria for the detection of tropical cyclones in climate
694 models and reanalyses. *J. Climate*, **20,** 2307-2314.

695 Wing, A. A., K. Emanuel, C. E. Holloway, and C. Muller, 2017: Convective self-aggregation in
696 numerical simulations: A review. *Surv. Geophys.*, doi: 10.1007/s10712-017-9408-4.

697 Yamaguchi, M., J. C. L. Chan, I.-J. Moon, K. Yoshida, and R. Mizuta, 2020: Global warming
698 changes tropical cyclone translation speed. *Nat Commun*, **11,** 47, doi:10.1038/s41467-
699 019-13902-y.

Zhang, G., H. Murakami, T. R. Knutson, R. Mizuta, and K. Yoshida, 2020: Tropical cyclone motion in a changing climate. *Sci Adv*, **6,** eaaz7610, doi:10.1126/sciadv.aaz7610.

704 **Table 1**

705 List of CMIP6 models used in the downscaling of tropical cyclones, including resolution of
706 atmospheric data and principal references

Institution	Model	Atmospheric Resolution[7]	Reference
Canadian Centre for Climate Modelling and Analysis	CanESM5	2.8 x 2.8 degrees	(Swart et al., 2019)
Centre National de Recherches Météorologiques	CNRM-CM6-1	1.4 x 1.4 degrees	(Voldoire et al., 2019)
National Center for Atmospheric Research	CESM2	1.25 x 0.93 degrees	(Danabasoglu et al., 2020)
EC-Earth consortium	EC-Earth3	0.7 x 0.7 degrees	
United Kingsom Met Office Hadley Centre	HadGEM3-GC31-LL	1.25 x 1.88 degrees	(Sellar et al., 2020)
Institut Pierre Simon Laplace	IPSL-CM6A-LR	1.25 x 2.5 degrees	(Hourdin et al., 2016)
Center for Climate System Research; University of Tokyo;Japan Agency for Marine-Earth Science and Technology; National Institute for Environmental Studies	MIROC6	1.4 x 1.4 degrees	(Tatebe et al., 2019)
Max Planck Institute	MPI-ESM1-2-HR	0.94 x 0.94 degree	(Müller et al., 2018)
United Kingsom Met Office	UKESM1-0-LL	1.25 x 1.875 degrees	(Sellar et al., 2020)

707

708

[7] This is the resolution of the output used to drive the downscaling; it may not correspond exactly with the native resolution of the GCM.

709 **Table 2**

710 Historical periods mean and linear trends over the historical period and over the $1\%\, yr^{-1}$ CO_2
711 increase experiment, expressed in percent change per CO_2 doubling. P-values less than 0.01 for
712 all trends except Cat 2 frequencies, where they are both 0.02.

713

Quantity	Historical Mean	Change over historical period	$1\%\,\mathrm{yr}^{-1}$ CO_2 (change per doubling)
Overall Frequency (yr^{-1})	84	9%	18%
Hurricane Frequency (yr^{-1})	57	10%	17%
Cat 1 Frequency (yr^{-1})	17	5%	8%
Cat 2 Frequency (yr^{-1})	10	5%	4%
Cat 3 Frequency (yr^{-1})	10	8%	7%
Cat 4 Frequency (yr^{-1})	10	13%	26%
Cat 5 Frequency (yr^{-1})	11	20%	44%
Major Hurricanes (yr^{-1})	32	14%	26%
Overall Landfall Frequency (yr^{-1})	48	7%	17%
Power Dissipation Index (m^3s^{-2})	3.9×10^{12}	15%	29%
Landfalling power dissipation (m^3s^{-3})	3.3×10^{10}	9%	25%
Radius of Maximum Winds (km)	59	2%	11%
Outer Radius (km)	630	3%	7%

714

715

716 **Figure Captions**

717

718 Figure 1: Annual probability density (green) and damage multiplied by probability density
719 (violet) based on 6200 U.S. landfalling synthetic tropical cyclones downscaled from the
720 MIROC 6 global coupled climate model for each of two periods: 1984-2014 from
721 historical simulations (solid) and 2070-2100 from the Shard Socioeconomic Pathway
722 (SSP) 5 (dashed). The probability density is per unit base 10 log of the damage. The
723 damage is to a portfolio of insured property in the eastern U.S. and is proportional to
724 the area under the violet curves.

725 Figure 2: Annual global frequency of downscaled tropical cyclones. Solid curves represent multi-
726 model means and shading indicates one standard deviation up and down. Dashed lines
727 show linear regression trends. Blue indicates the historical period 1850-2014 while red
728 shows the $1\%\ yr^{-1}$ CO_2 increase experiment arbitrarily beginning in 1970. Green curves
729 show the multi-model mean, globally summed genesis potential index (GPI).

730 Figure 3: a) Global number of tropical cyclones by Saffir-Simpson category of lifetime maximum
731 intensity. Tropical storms here include only events with maximum intensities of at least
732 40 kts. Black indicates observed (IBTrACS) during the period 1980-2018, while
733 downscaled events are shown in blue for the historical period and red from the linear
734 regressions of trends in the $1\%\ yr^{-1}$ simulations at the time of CO_2 doubling. The
735 downscaled events are multi-model means. b) As is a) but observed intensities have
736 been increased by 10%.

737 Figure 4: As in Figure 2 but showing the power dissipation index

738 Figure 5: As in Figure 2 but showing the landfall power dissipation index

739 Figure 6: Genesis density (top row), track density (middle row) and power dissipation density
740 (bottom row) from IBTrACS data, 1979-2015 (a-c), the multi-model mean over the
741 historical period (d-f) and percentage change from the historical period to the mean of
742 the $1\%\, yr^{-1}$ simulation (g-i). The changes are only displayed where 7 or more of the
743 models agree on the sign of the change.

744 Figure 7: a) Base 10 logarithm of the multi-model mean probability density of intensification
745 and dissipation rates of downscaled tropical cyclones over the historical period (blue)
746 and the $1\%\, yr^{-1}$ simulations (red). The shading shows one standard deviation up and
747 down from the mean among the models. b) Percentage change between the historical
748 and $1\%\, yr^{-1}$ simulations. Shading shows one standard deviation up and down from the
749 mean change among the models.

750 Figure 8: Multi-model mean translation speed (kts) for the historical period (a) and the change
751 after a doubling of CO_2 (b). The latter is displayed only where at least 7 of the 9
752 downscaled models agree on the sign of the change.

753 Figure 9: Time series of annual tropical cyclone counts for the standard downscaling of the
754 UKMO model (blue) and with the imposition of an artificial vorticity threshold (red).
755 Dashed lines show the linear regressions.

Figure 10: The terms on the right side of (4); respectively vorticity, χ, potential intensity (PI), and shear. The black curve shows their sum while the green curve shows the logarithm of the actual GPI. Each quantity is relative to its initial value.

Figure 11: Change in the annual global frequency of tropical cyclones of 6 Saffir-Simpson categories. The blue bars show changes in explicitly simulated tropical cyclones in the HiFLOR model and the red bars show changes in events downscaled from HiFLOR.

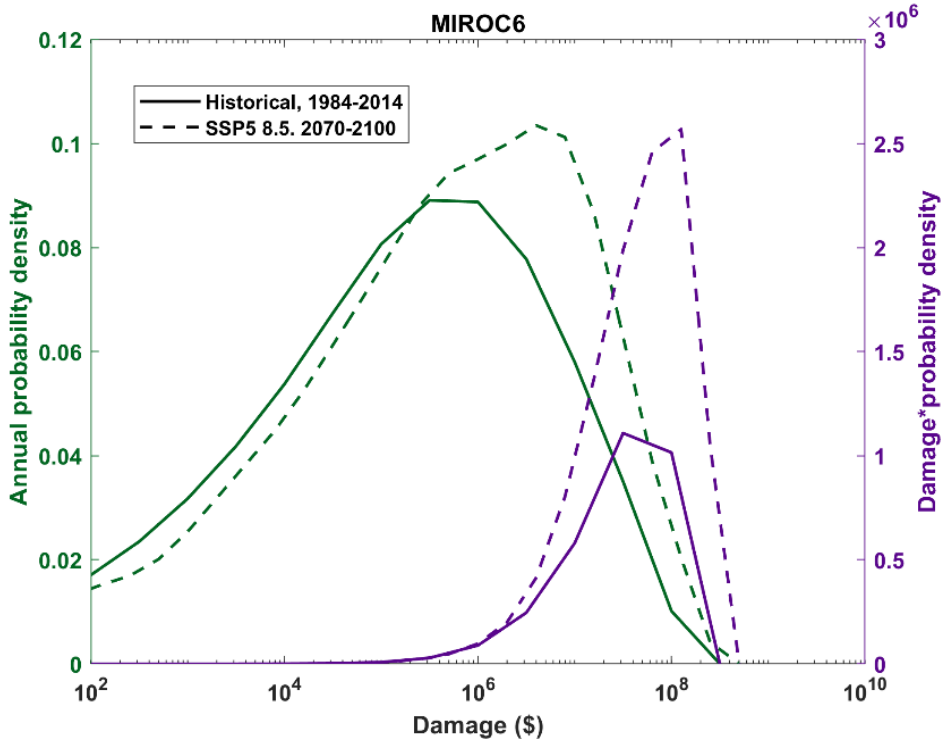

Figure 1: Annual probability density (green) and damage multiplied by probability density (violet) based on 6200 U.S. landfalling synthetic tropical cyclones downscaled from the MIROC 6 global coupled climate model for each of two periods: 1984-2014 from historical simulations (solid) and 2070-2100 from the Shard Socioeconomic Pathway (SSP) 5 (dashed). The probability density is per unit base 10 log of the damage. The damage is to a portfolio of insured property in the eastern U.S. and is proportional to the area under the violet curves.

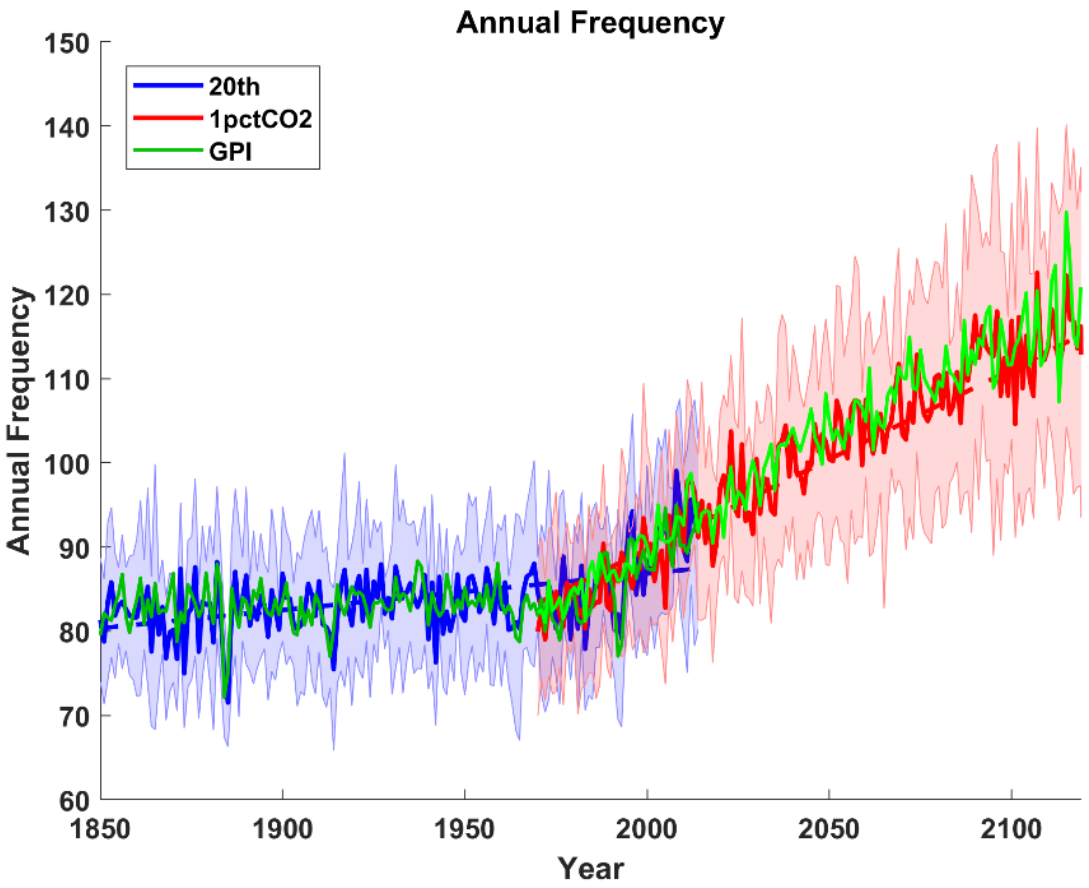

Figure 2: Annual global frequency of downscaled tropical cyclones. Solid curves represent multi-model means and shading indicates one standard deviation up and down. Dashed lines show linear regression trends. Blue indicates the historical period 1850-2014 while red shows the $1\%\ yr^{-1}$ CO_2 increase experiment arbitrarily beginning in 1970. Green curves show the multi-model mean, globally summed genesis potential index (GPI).

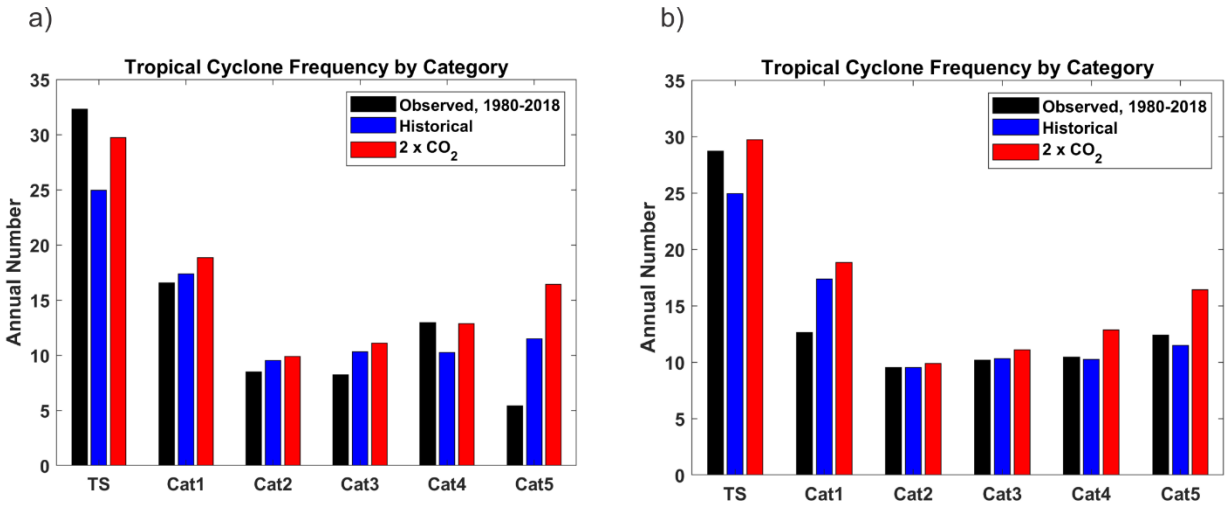

Figure 3: a) Global number of tropical cyclones by Saffir-Simpson category of lifetime maximum intensity. Tropical storms here include only events with maximum intensities of at least 40 kts. Black indicates observed (IBTrACS) during the period 1980-2018, while downscaled events are shown in blue for the historical period and red from the linear regressions of trends in the $1\%\, yr^{-1}$ simulations at the time of CO_2 doubling. The downscaled events are multi-model means. b) As is a) but observed intensities have been increased by 10%.

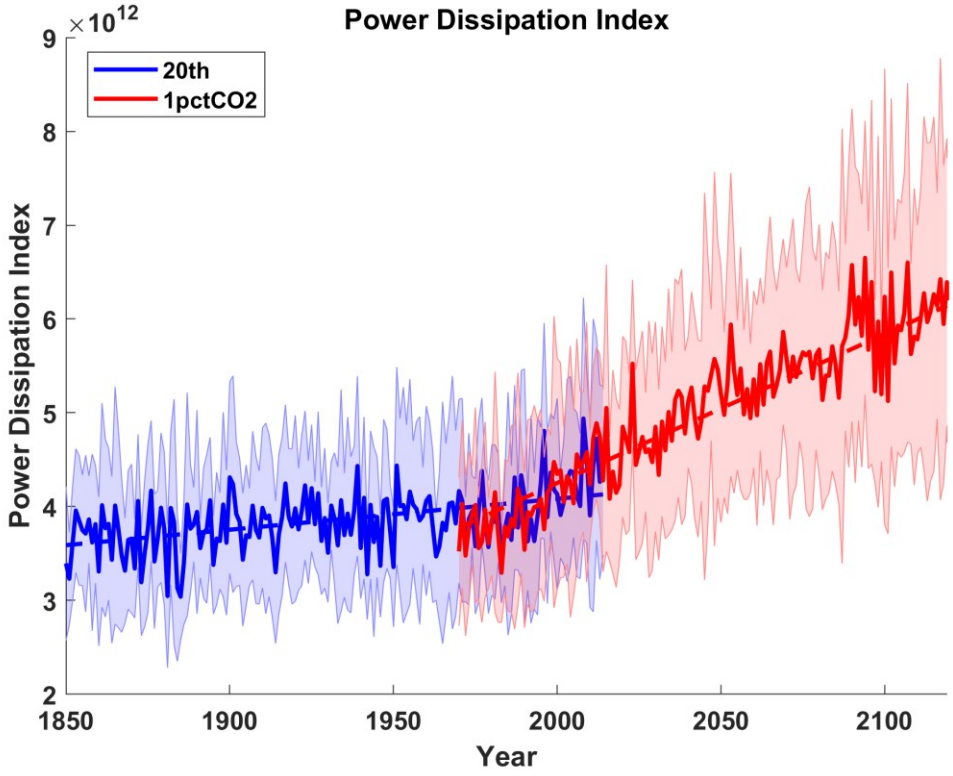

Figure 4: As in Figure 2 but showing the power dissipation index

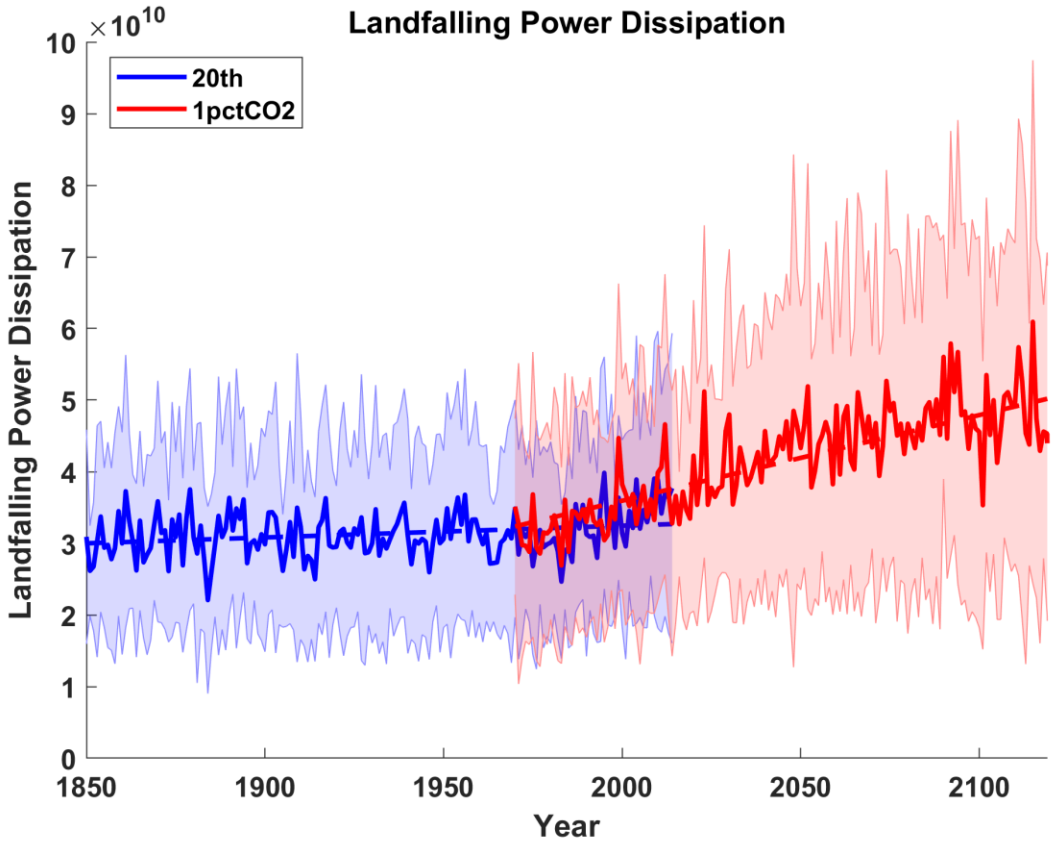

Figure 5: As in Figure 2 but showing the landfall power dissipation index

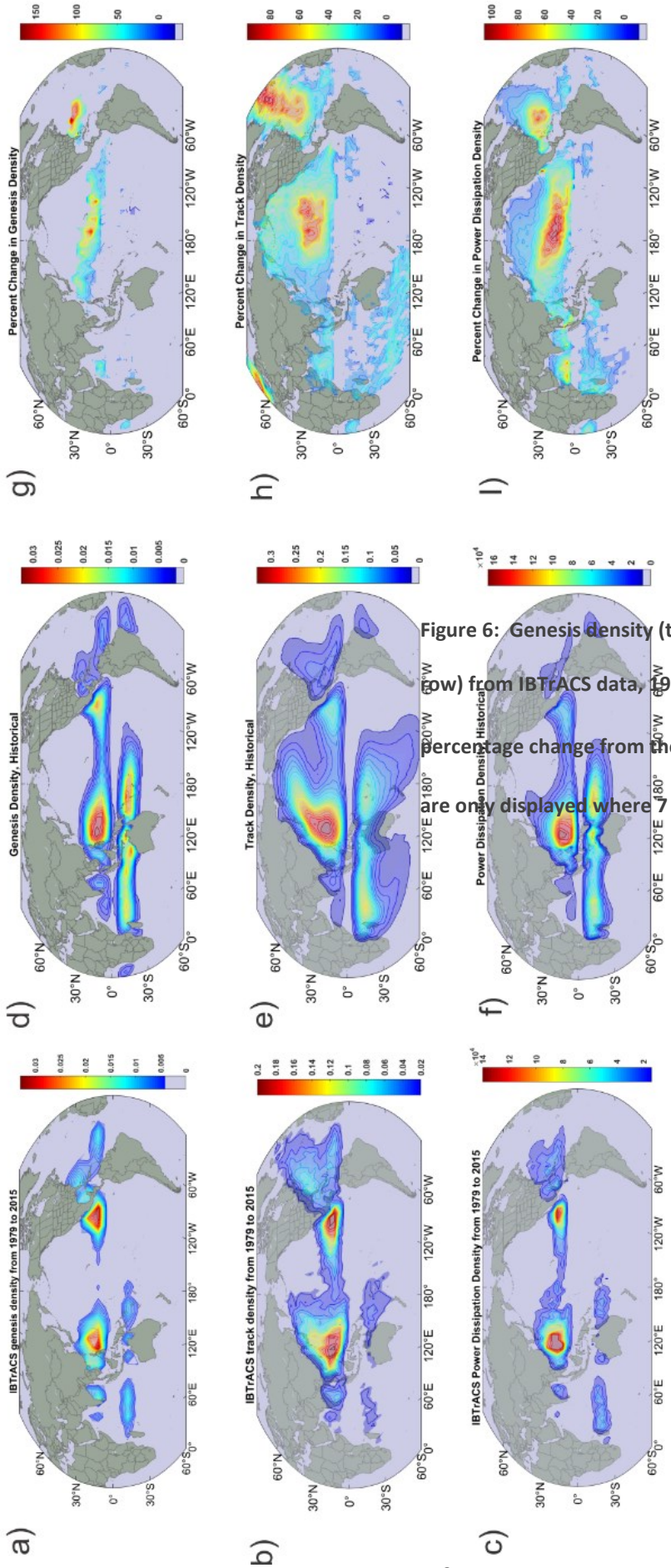

Figure 6: Genesis density (top row), track density (middle row) and power d

row) from IBTrACS data, 1979-2015 (a-c), the multi-model mean over the his

percentage change from the historical period to the mean of the $1\%\ yr^{-1}$ s

are only displayed where 7 or more of the models agree on the sign of the cl

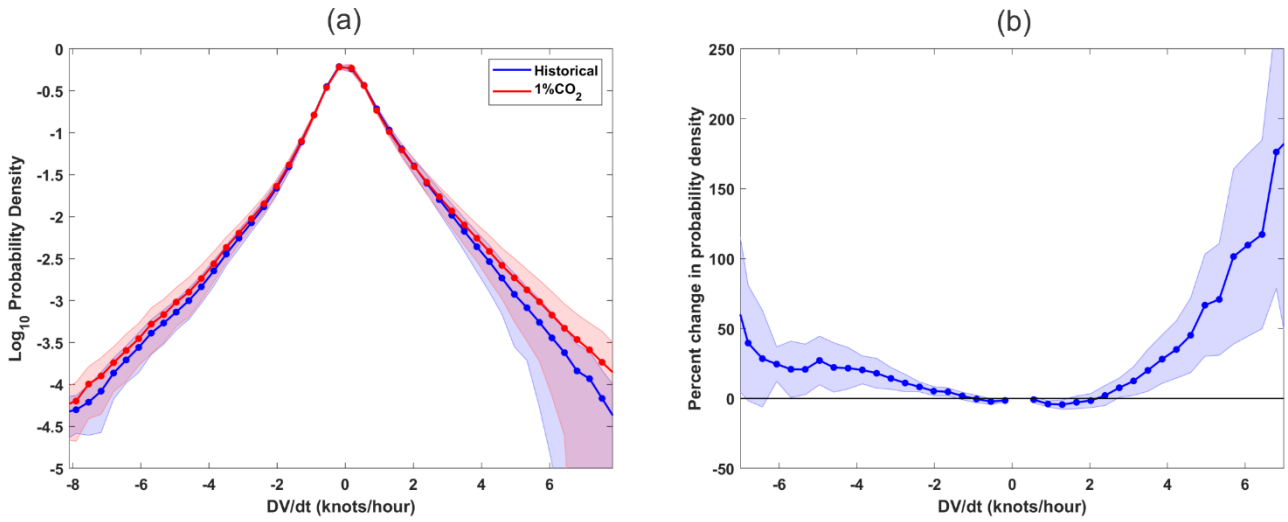

Figure 7: a) Base 10 logarithm of the multi-model mean probability density of intensification and dissipation rates of downscaled tropical cyclones over the historical period (blue) and the $1\%\, yr^{-1}$ simulations (red). The shading shows one standard deviation up and down from the mean among the models. b) Percentage change between the historical and $1\%\, yr^{-1}$ simulations. Shading shows one standard deviation up and down from the mean change among the models.

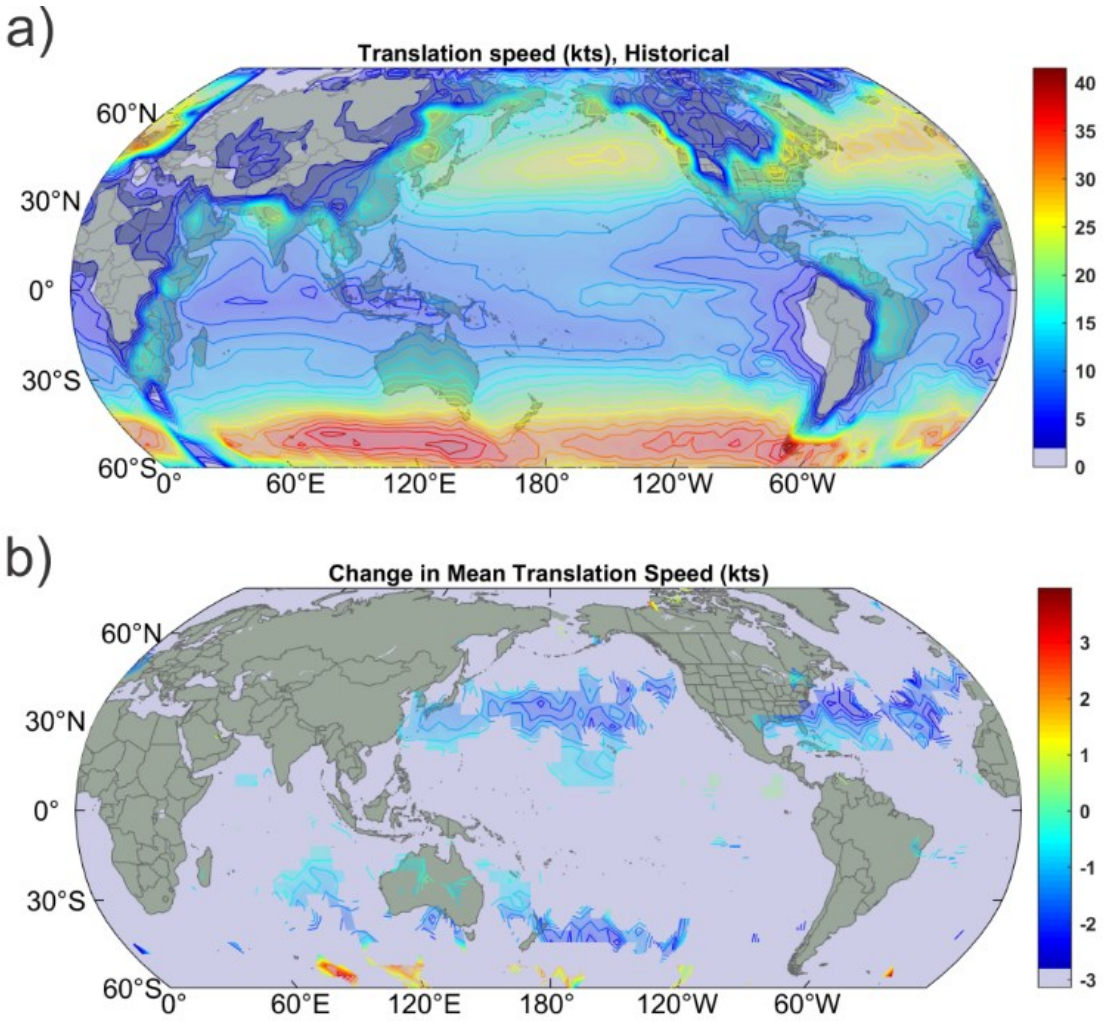

868

869

870 **Figure 8: Multi-model mean translation speed (kts) for the historical period (a) and the change after a doubling**

871 **of CO_2 (b). The latter is displayed only where at least 7 of the 9 downscaled models agree on the sign of the**

872 **change.**

873

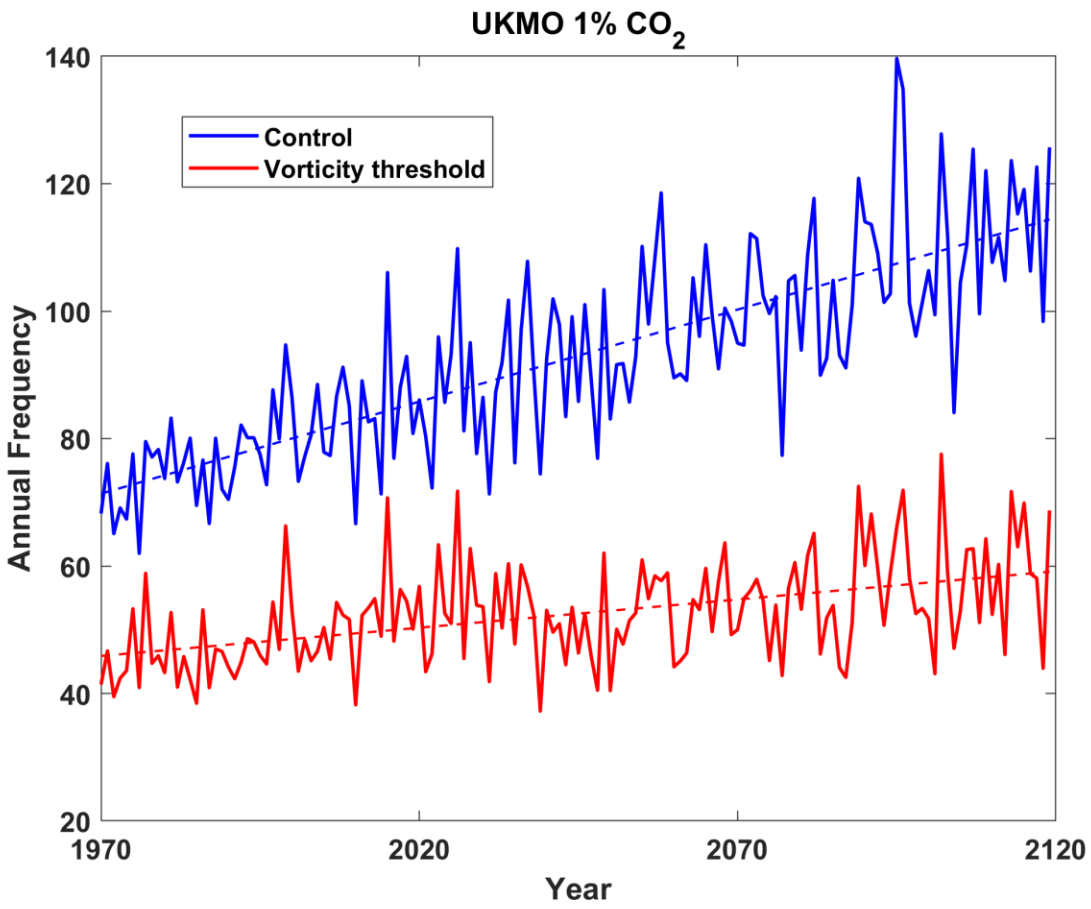

874

875 **Figure 9: Time series of annual tropical cyclone counts for the standard downscaling of the UKMO model (blue)**

876 **and with the imposition of an artificial vorticity threshold (red). Dashed lines show the linear regressions.**

877

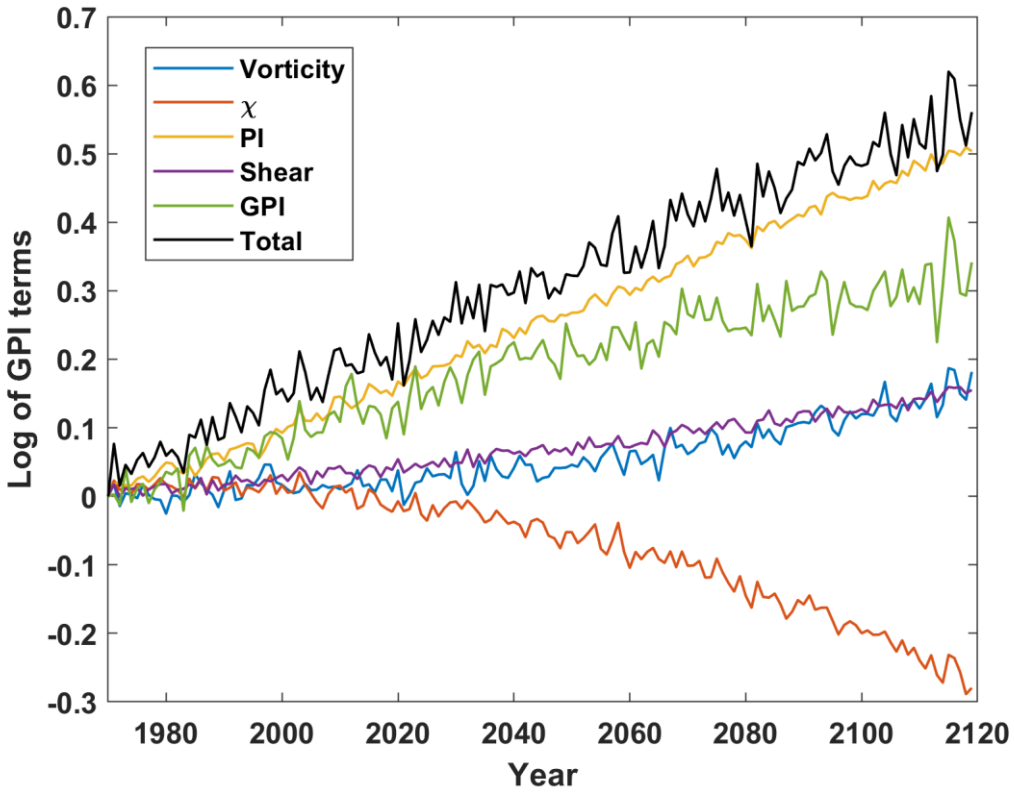

878

Figure 10: The terms on the right side of (4); respectively vorticity, χ, potential intensity (PI), and shear. The black curve shows their sum while the green curve shows the logarithm of the actual GPI. Each quantity is relative to its initial value.

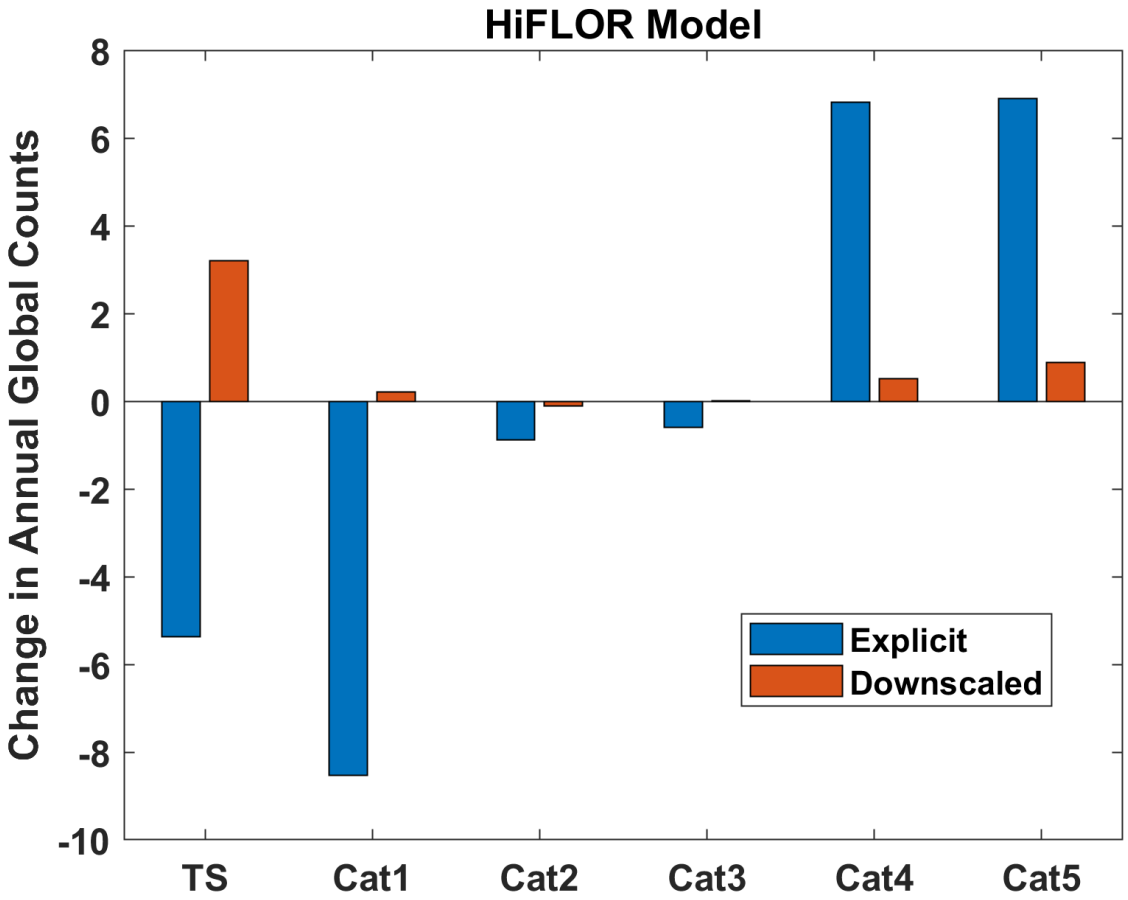

879

880 **Figure 11: Change in the annual global frequency of tropical cyclones of 6 Saffir-Simpson categories. The blue**

881 **bars show changes in explicitly simulated tropical cyclones in the HiFLOR model and the red bars show changes**

882 **in events downscaled from HiFLOR.**

883